

Nucleon energy correlators as a probe of light-quark dipole operators at the EIC

Yingsheng Huang,^{1,2,*} Xuan-Bo Tong,^{3,4,†} and Hao-Lin Wang^{5,6,‡}

¹*School of Physics, Central South University, Changsha 410083, China*

²*Department of Physics and Astronomy, University of Utah, Salt Lake City, UT 84112, USA*

³*Department of Physics, University of Jyväskylä,
P.O. Box 35, 40014 University of Jyväskylä, Finland*

⁴*Helsinki Institute of Physics, P.O. Box 64, 00014 University of Helsinki, Finland*

⁵*State Key Laboratory of Nuclear Physics and Technology, Institute of Quantum Matter,
South China Normal University, Guangzhou 510006, China*

⁶*Guangdong Basic Research Center of Excellence for Structure and Fundamental Interactions of Matter,
Guangdong Provincial Key Laboratory of Nuclear Science, Guangzhou 510006, China*

We propose nucleon energy correlators (NECs) as a novel framework to probe electroweak light-quark dipole operators in deep inelastic scattering with an unpolarized nucleon. These operators encode chirality-flipping interactions, whose effects are usually quadratically suppressed in unpolarized cross sections. We construct a chiral-odd quark NEC that accesses quark transverse spin via azimuthal angle asymmetries in the energy flow of the target fragmentation region. These asymmetries serve as clean and powerful observables, enabling linear constraints on the quark dipole couplings. Unlike existing methods, our approach requires neither polarized nucleon beams nor final-state hadron identification, relying instead on fully inclusive calorimetric measurements. This work establishes one of the first applications of energy correlator observables to new physics searches and opens a promising direction for precision studies of chirality-flipping effects at electron-ion colliders.

Introduction The search for new physics (NP) beyond the standard model (SM) has been a major focus of collider experiments such as the Large Hadron Collider (LHC). The lack of direct signals suggests that NP may emerge at an energy scale Λ well beyond the current experimental reach. The standard model effective field theory (SMEFT) offers a systematic framework to describe such NP effects via higher-dimensional operators built from SM fields [1–3]. Among these, dimension-6 electroweak (EW) dipole operators involving light fermions are particularly intriguing for their chirality-flipping structure¹ [4–19], which is highly suppressed in the SM but essential for understanding electromagnetic dipole moments of leptons and baryons [20–35]. However, constraints on these operators remain weak because the interference between dipole and SM amplitudes, scaling as $\mathcal{O}(\Lambda^{-2})$, typically vanishes in unpolarized observables [8–15]. Consequently, the leading effects arise at $\mathcal{O}(\Lambda^{-4})$, resulting in reduced sensitivity and contamination from dimension-8 operators.

A new strategy to overcome this issue was recently proposed in [16, 17], which leverages the transverse spin of fermions. Since transverse spin states are superpositions of helicity eigenstates, they enable interference between opposite-helicity components, restoring sensitivity to the dipole-SM interference at $\mathcal{O}(\Lambda^{-2})$. Building on this insight, several observables have been designed for the Electron-Ion Collider (EIC), the LHC, and future lepton colliders [16–19, 36]. While transverse polarization of electron beams can be generated and controlled

in accelerators, accessing transversely polarized quarks is more difficult due to color confinement. Existing approaches require non-perturbative correlations between quark spin and a transverse reference vector, either via nucleon polarization or via the transverse momenta of final-state hadrons, encoded in transversity parton distribution functions (PDFs) and dihadron fragmentation functions [16, 18]. Nevertheless, these methods either demand polarized nucleon beams, which compromise luminosity, or rely on semi-inclusive measurements that require particle identification and multi-particle tracking.

To address these limitations, we propose nucleon energy correlators (NECs) as an innovative approach to probe light-quark EW dipole operators in inclusive deep inelastic scattering (DIS) with an unpolarized nucleon. Recently introduced in [37] as an extension of energy correlators from final-state jets to nucleon structure, NECs enable the imaging of partonic dynamics through correlations between initial-state partons and energy flux in the target fragmentation region (TFR) [37–46] (see [47] for a review). By exploiting these correlations, we construct a chiral-odd quark NEC that accesses the quark transverse spin inside an unpolarized nucleon. This NEC ensures a nonzero interference between the dipole and SM amplitudes, generating unique azimuthal asymmetries in the energy distribution in DIS. We demonstrate that these asymmetries exhibit clean and strong sensitivity to quark dipole couplings. Crucially, our method works without polarized nucleon beams and requires only inclusive calorimetric measurements, making it an exceptional observable for probing chirality-flipping interactions at both existing and future electron-ion colliders.

Quark transversity NEC Let us begin by considering

¹ See, e.g., the quark dipole operator $(\bar{Q}\sigma^{\mu\nu}d)HB_{\mu\nu}$ in Eq. (8).

quark NECs in an unpolarized nucleon, which moves rapidly along the $+\hat{z}$ direction with momentum P . The associated NECs are encoded in the following correlation function [37, 42]:

$$\mathcal{M}^{[\Gamma]}(x, \theta, \phi) = \int \frac{d\eta^-}{4\pi} e^{-ixP^+\eta^-} \times \langle P | \bar{\psi}(\eta^-) \mathcal{L}_n^\dagger(\eta^-) \Gamma \mathcal{E}(\theta, \phi) \mathcal{L}_n(0) \psi(0) | P \rangle, \quad (1)$$

which describes the conditional probability of finding a quark with the longitudinal momentum fraction x inside the target nucleon, given the observation of an energy flux at the solid angle (θ, ϕ) in the TFR. θ and ϕ denote the polar and azimuthal angles, respectively. Formally, the quark NECs can be viewed as the collinear PDFs modified by the insertion of the energy flow operator $\mathcal{E}(\theta, \phi)$, which is defined through its action on hadronic states [48, 49]

$$\mathcal{E}(\theta, \phi) | X \rangle = \sum_{i \in X} \frac{E_i}{E_N} \delta(\theta_i^2 - \theta^2) \delta(\phi_i - \phi) | X \rangle, \quad (2)$$

where E_i denotes the energy of hadron i , normalized by the nucleon energy E_N . Here, we use the light-cone coordinates defined as $a^\mu = (a^+, a^-, \vec{a}_\perp) = ((a^0 + a^3)/\sqrt{2}, (a^0 - a^3)/\sqrt{2}, a^1, a^2)$, and \mathcal{L}_n denotes the light-cone gauge link.

The correlation function $\mathcal{M}^{[\Gamma]}$ depends on the choice of the Dirac matrix Γ , which selects specific quark spin components. For instance, the leading-twist unpolarized quark NEC is obtained with $\Gamma = \gamma^+$:

$$f_1^q(x, \theta^2) = \mathcal{M}^{[\gamma^+]}(x, \theta, \phi), \quad (3)$$

which is chiral-even and rotationally invariant in the transverse plane [37].

While prior studies have primarily focused on the chiral-even NECs [37–43] (see a systematic classification in [42]), we extend the formalism to the chiral-odd components. In particular, the quark transversity NEC can be obtained by using the projector $\Gamma^\alpha = i\sigma^{\alpha+}\gamma_5$ with $\alpha = 1, 2$, analogous to that used for transversity PDFs. However, unlike transversity PDFs, which requires a transversely polarized nucleon [50], NECs can access the quark transverse spin even in an *unpolarized* nucleon, owing to the azimuthal dependence of the observed energy flux.

To explicitly illustrate this feature, we introduce the vector $n_T^\mu = (0, 0, \sin\theta \cos\phi, \sin\theta \sin\phi)$ to specify the transverse direction of the observed energy flux. Then the quark transversity NEC $h_1^{t,q}(x, \theta^2)$ is defined as

$$\frac{\epsilon_\perp^{\alpha\rho} n_{T,\rho}}{|n_T|} h_1^{t,q}(x, \theta^2) = \mathcal{M}^{[i\sigma^{\alpha+}\gamma_5]}(x, \theta, \phi), \quad (4)$$

where $\epsilon_\perp^{\mu\nu} = \epsilon^{\mu\nu-+}$ with $\epsilon^{0123} = 1$. This equation shows that $h_1^t(x, \theta^2)$ captures azimuthal correlations between

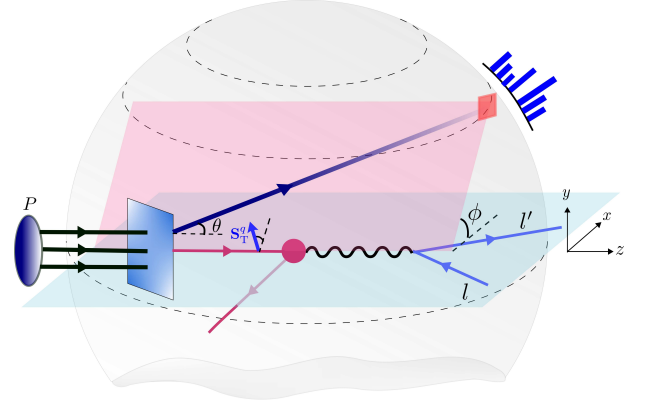


FIG. 1. Illustration of the NEC mechanism for probing the SMEFT quark dipole operator in DIS. The blue transverse plate highlights the role of the transversity NEC, which selects the quark transverse spin S_T^q in an unpolarized nucleon by measuring an energy flux from the target remnants. The magenta blob denotes the dipole interaction mediated by γ or Z . The interference with the SM amplitude is implied.

the quark's transverse polarization and the energy flow direction. Physically, it describes the difference in probability of finding a quark polarized along the transverse direction of the energy flow versus in the opposite direction. Being chiral-odd, the transversity NEC is off-diagonal in the helicity basis and naturally induces interference between amplitudes of opposite quark helicities. This provides a novel mechanism for generating chirality-flipping effects, enabling probes of dipole operators in unpolarized nucleon scatterings.

Probing the quark dipole operators with transversity NEC

To demonstrate how the transversity NEC probes the SMEFT dipole couplings, we consider the energy pattern within the TFR in inclusive DIS with an unpolarized nucleon, $l + p \rightarrow l' + X$. Experimentally, this observable is determined from the angular distribution of the total energy deposited in the calorimeters. Following Refs. [37, 42], we define the energy pattern cross section as:

$$\Sigma(\theta, \phi) = \sum_{i \in X} \int d\sigma^{l+p \rightarrow l'+X} \frac{E_i}{E_N} \delta(\theta^2 - \theta_i^2) \delta(\phi - \phi_i). \quad (5)$$

We work in the Breit frame, where the momentum transfer ($q = l' - l$) is aligned along the $-\hat{z}$ direction, and the nucleon moves in the opposite direction. As shown in Fig. 1, the polar angle θ is measured with respect to the nucleon beam, and the azimuthal angle ϕ is defined relative to the lepton scattering plane. The standard DIS kinematic variables are also used: the photon virtuality $Q^2 = -q^2$, the Bjorken variable $x_B = Q^2/(2P \cdot q)$, and the inelasticity $y = Q^2/(sx_B)$ with \sqrt{s} denoting the center-of-mass energy of the ep collision.

Let us first consider the case of an unpolarized electron beam. We are particularly interested in the following

azimuthal modulations of the energy pattern:

$$\Sigma(\theta, \phi) = \Sigma_{UU}(\theta) + \Sigma_{UU}^{\sin \phi}(\theta) \sin \phi + \Sigma_{UU}^{\cos \phi}(\theta) \cos \phi. \quad (6)$$

We focus on the TFR, characterized by small polar angles ($\theta Q \ll Q$), where the energy flux originates from the fragmentation of target remnants. Following the general arguments in [38, 42], the energy pattern cross section in this region factorizes into hard partonic scattering coefficients and the non-perturbative NECs, defined by Eq. (1). Because NECs encapsulate all the information regarding the energy flow, including its azimuthal ϕ dependence, the ϕ -independent cross section Σ_{UU} factorizes with unpolarized NECs, such as f_1 given in Eq. (3). By contrast, the ϕ -dependent terms $\Sigma_{UU}^{\sin \phi}$ and $\Sigma_{UU}^{\cos \phi}$ are expected to factorize with the transversity NEC h_1^t , which encodes azimuthal correlations as seen in Eq. (4). Remarkably, after factorization, the hard scatterings remain the same as in standard inclusive DIS process [42].

Within the SM, the energy pattern is isotropic in the transverse plane. Since quark helicity flip in DIS hard scattering is suppressed by light quark masses, only the chiral-even unpolarized quark NEC $f_1(x, \theta^2)$ contributes to $\Sigma(\theta, \phi)$ in the massless limit, while the chiral-odd contributions from the transversity NEC $h_1^t(x, \theta^2)$ vanish to all orders in α_s . The only non-zero contribution arises from the azimuthally independent cross section Σ_{UU} . At leading order in α_s , the contribution from the photon exchanges takes the following form:

$$\frac{d\Sigma_{UU}}{dx_B dQ^2} = \frac{2\pi\alpha_{\text{em}}^2}{Q^4} (y^2 - 2y + 2) \sum_q Q_q^2 f_1^q(x_B, \theta^2), \quad (7)$$

where $\alpha_{\text{em}} = e^2/(4\pi)$ is the fine structure constant and Q_q is the quark electric charge.

Although the $\sin \phi$ and $\cos \phi$ azimuthal modulations are absent within the SM, they could arise from chirality-flipping NP effects, such as the following dimension-6 SMEFT dipole interactions [3]:

$$\begin{aligned} \mathcal{L} = & \frac{1}{\Lambda^2} \left[C_{uW} (\bar{Q}\sigma^{\mu\nu} u) \tau^I \tilde{H} W_{\mu\nu}^I + C_{uB} (\bar{Q}\sigma^{\mu\nu} u) \tilde{H} B_{\mu\nu} \right. \\ & \left. + C_{dW} (\bar{Q}\sigma^{\mu\nu} d) \tau^I H W_{\mu\nu}^I + C_{dB} (\bar{Q}\sigma^{\mu\nu} d) H B_{\mu\nu} \right] + \text{h.c.}, \end{aligned} \quad (8)$$

where τ^I are the Pauli matrices, and $\tilde{H}_I = \epsilon_{IJ} H^J$. The field strength tensors $W_{\mu\nu}^I$ and $B_{\mu\nu}$ correspond to the $SU(2)_L$ and $U(1)_Y$ gauge fields, respectively. Here, Q denotes the left-handed quark doublet, while u and d represent the right-handed up- and down-type quark singlets. In this work, we restrict our attention to operators involving only the first generation and define their dipole couplings to photon and Z -boson c_i as

$$\begin{aligned} c_{q\gamma} &= (v/\sqrt{2}\Lambda^2) (c_W C_{qB} \pm s_W C_{qW}), \\ c_{qZ} &= (v/\sqrt{2}\Lambda^2) (-s_W C_{qB} \pm c_W C_{qW}). \end{aligned} \quad (9)$$

The plus (minus) sign is for the up (down) quark, $c_W = \cos \theta_W$ and $s_W = \sin \theta_W$ with θ_W being the Weinberg angle, and v is the Higgs vacuum expectation value.

As illustrated in Fig. 1, these azimuthal modulations originate from the interplay between the SMEFT dipole operator and the quark transversity NEC $h_1^t(x, \theta^2)$. Being inherently chiral-odd, the dipole interaction induces a quark helicity flip during the hard scattering with the virtual photon or Z -boson. As a result, the dominant contributions emerge from the interference between the helicity-conserving SM amplitude and the helicity-flipping SMEFT amplitude at $\mathcal{O}(\Lambda^{-2})$. Such interference necessarily couples to a chiral-odd quark NEC, namely the transversity NEC. As revealed in Eq. (4), the quark transverse spin is accessed through intrinsic azimuthal correlations with the energy flux direction \vec{n}_T , thereby yielding distinct $\sin \phi$ and $\cos \phi$ modulations. Furthermore, these asymmetries are uniquely generated by the dipole operators, as other dimension-6 SMEFT operators either require transverse electron polarization or are suppressed by the electron Yukawa coupling.

We find that the $\sin \phi$ -modulation is determined by the real parts of the quark dipole couplings $c_{q\gamma}$ and c_{qZ} through the interference between photon and Z -boson exchanges. The corresponding cross section is given by:

$$\begin{aligned} \frac{d\Sigma_{UU}^{\sin \phi}}{dx_B dQ^2} &= \frac{4\pi\alpha_{\text{em}}^2}{ec_W s_W} \frac{y\sqrt{1-y}}{Q(Q^2 + m_Z^2)} \sum_q h_1^{t,q}(x_B, \theta^2) \quad (10) \\ &\times \left\{ \left[\frac{2-y}{y} g_A^q g_V^e + g_V^q g_A^e \right] \frac{\text{Re}[c_{q\gamma}]}{c_W s_W} - Q_q g_A^e \text{Re}[c_{qZ}] \right\}, \end{aligned}$$

where $g_V^f = T_f^3/2 - Q_f s_W^2$ and $g_A^f = T_f^3/2$ are the vector and axial-vector couplings with T^3 as the third component of weak isospin. Similarly, the $\cos \phi$ -modulation is sensitive to the imaginary parts of the dipole couplings and can be obtained from Eq. (10) by replacing $\text{Re}[c_{q\gamma, Z}]$ with $-\text{Im}[c_{q\gamma, Z}]$. The anti-quark components in Eq. (7) and Eq. (10) can be obtained by taking $g_A^q \rightarrow -g_A^q$. Considering the EIC kinematics, we have neglected pure Z -boson exchanges.

Our analysis can be readily generalized to include a longitudinally polarized electron beam, yielding the cross section $\Sigma_{LU}^{\sin \phi(\cos \phi)}$ factorized in terms of the transversity NEC h_1^t . Owing to the parity violation induced by electron polarization, the azimuthal modulations can be generated via $\gamma\gamma$ interference, without Q^2/m_Z^2 suppression present in the unpolarized case $\Sigma_{UU}^{\sin \phi(\cos \phi)}$. As indicated later, this leads to an enhanced sensitivity to the dipole couplings. Complete analytical results are provided in the Supplemental Material [51].

Calorimetric asymmetries and the non-perturbative input
To quantify the effects of the SMEFT dipole operators, we introduce azimuthal angle asymmetries of the energy pattern. For an unpolarized electron beam, these are purely calorimetric asymmetries defined with respect to

the lepton scattering plane:

$$A_{UU}^u = \frac{\pi}{2} \frac{\Sigma(u > 0) - \Sigma(u < 0)}{\Sigma(u > 0) + \Sigma(u < 0)}, \quad (11)$$

where u is taken to be either $\sin\phi$ or $\cos\phi$, isolating the real or imaginary part of the dipole couplings, respectively. $\Sigma(u > 0)$ represents the energy pattern cross section integrated over the region with $u > 0$:

$$\Sigma(u > 0) \equiv \int_{\theta_{\min}^2}^{\theta_{\max}^2} d\theta^2 w(\theta) \int_0^{2\pi} d\phi \Sigma(\theta, \phi) \Theta(u), \quad (12)$$

and similarly for $u < 0$. The polar-angle weight function $w(\theta)$ is introduced for later use. For a longitudinally polarized electron beam, one can analogously define the asymmetries A_{LU}^u by combining the calorimetric asymmetry with the longitudinal spin asymmetry, as we specify in [51].

Numerical evaluation of these asymmetries requires non-perturbative input for the quark NECs f_1 and h_1^t . While the unpolarized quark NEC f_1 can be extracted directly from Σ_{UU} in the TFR [37], one can also measure the transversity NEC h_1^t without assuming SMEFT interactions by tagging an additional hadron in the current fragmentation region. Such measurements are feasible at facilities including HERA, JLab, and the EIC.

Although direct experimental determinations of NECs are not yet available, a remarkable correspondence has been established between θ -weighted moments of the NECs and k_{\perp} -weighted moments of transverse-momentum-dependent parton distributions (TMDs), including the unpolarized quark NEC [41]. This correspondence can be straightforwardly extended to the transversity NEC. Specifically, we have

$$\begin{aligned} E_N \int d\theta^2 |\sin\theta| f_1(x, \theta^2) &= \int \frac{d^2 \mathbf{k}_{\perp}}{2\pi} |\mathbf{k}_{\perp}| f_1(x, \mathbf{k}_{\perp}^2), \\ E_N \int d\theta^2 |\sin\theta| h_1^t(x, \theta^2) &= \int \frac{d^2 \mathbf{k}_{\perp}}{2\pi} \frac{\mathbf{k}_{\perp}^2}{M} h_1^t(x, \mathbf{k}_{\perp}^2), \end{aligned} \quad (13)$$

where f_1 and h_1^t are the unpolarized and Boer-Mulder quark TMDs, respectively. These relations allow us to infer the NECs from existing global fits of TMDs. In our analysis, we adopt the parameterization from in [52], which assumes a Gaussian form for the k_{\perp} -dependence.

To utilize the above relations, in Eq. (12) we choose the θ -weight as $w(\theta) = |\sin\theta|$. The limits of the θ -integration are determined by both theoretical and experimental considerations. The upper bound θ_{\max} is imposed to ensure the validity of the factorization in the TFR [38, 42]. This corresponds to a transverse momentum cutoff $k_{\perp}^{\max} \sim Q\theta_{\max}$ in the k_{\perp} -integrals in Eq. (13). Due to rapid falloff of the Gaussian TMDs at large k_{\perp} , this cutoff has negligible numerical impact on the integral. The lower bound θ_{\min} is determined by the coverage

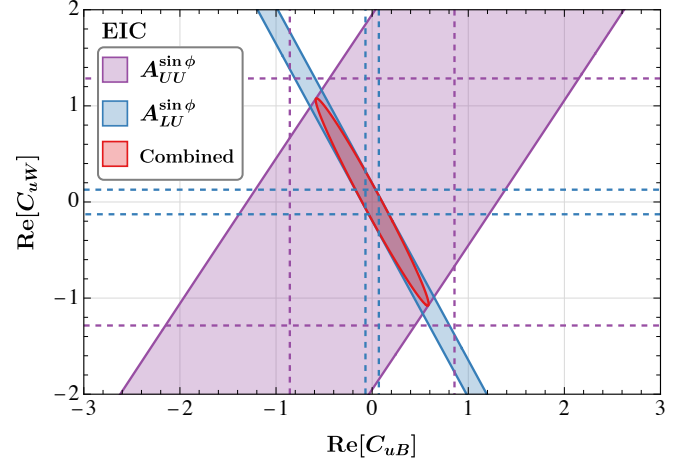


FIG. 2. Projected 68% C.L. constraints at the EIC on the two Wilson coefficients $\text{Re}[C_{uB}]$ and $\text{Re}[C_{uW}]$, assuming $\Lambda = 1$ TeV. The limits are derived from the azimuthal asymmetries $A_{UU}^{\sin\phi}$ (purple), $A_{LU}^{\sin\phi}$ (blue), and their combination (red). The shaded regions represent the simultaneous two-coefficient constraints, while dashed lines show the limits for a single coefficient.

of the calorimeter in the nucleon forward region. It imposes a minimal transverse-momentum threshold given by $k_{\perp}^{\min} \approx E_{\min}\theta_{\min}$, where E_{\min} characterizes the energy resolution of calorimeters [47]. Practically, we adopt $k_{\perp}^{\min} \approx 0$ GeV and $k_{\perp}^{\max} = 5$ GeV. With these inputs, we have evaluated numerically both $A_{UU}^{\sin\phi}$ and $A_{LU}^{\sin\phi}$ for the EIC kinematics, and the detailed results can be found in the Supplemental Material [51].

Projected sensitivity at the EIC Although the EIC is primarily designed for exploring parton physics, its clean experimental environment and high luminosity also offer great potential for probing NP effects [47]. To estimate the sensitivity to the dipole operators at the EIC, we perform a χ^2 analysis based on the predicted asymmetries. We select a representative EIC configuration [47] with a center-of-mass energy of $\sqrt{s} = 105$ GeV, which corresponds to the optimal integrated luminosity of $\mathcal{L} = 100 \text{ fb}^{-1}$. The analysis is carried out in Q bins for $Q \in [10, 60]$ GeV and $x \in [0.01, 0.5]$, incorporating an inelasticity cut $0.1 \leq y \leq 0.9$. We assume the experimental value consistent with the leading-twist SM prediction, and is negligible. With this setup, the statistical uncertainty $\delta A_i \simeq \pi/(2\sqrt{\mathcal{E}_{\text{total}}})$ is dominant over the systematic uncertainties. Here, $\mathcal{E}_{\text{total}} = (\Sigma(u > 0) + \Sigma(u < 0)) \times \mathcal{L}$ is the accumulated energy deposition.

Fig. 2 presents the projected constraints on the real parts of dimensionless Wilson coefficients C_{uW} and C_{uB} at 68% C.L. using $\sin\phi$ -asymmetry. Assuming single-operator dominance, $A_{UU}^{\sin\phi}$ constrain the Wilson coefficients almost at the $\mathcal{O}(1)$ level, as shown by the purple dashed lines. However, when both coefficients are considered simultaneously, the resulting constraint ellipse is

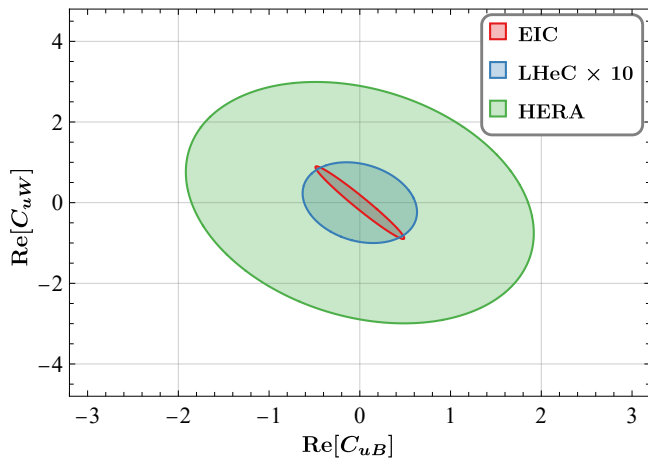


FIG. 3. Comparison of projected 68% C.L. constraints on $\text{Re}[C_{uB}]$ and $\text{Re}[C_{uW}]$ from HERA (green), the EIC (red), and the LHeC (blue), assuming $\Lambda = 1$ TeV. The LHeC limits are scaled by a factor of 10 for visibility. A detailed description of our analysis setup is provided in [51].

elongated into a purple band, indicating a strong correlation between C_{uW} and C_{uB} .

This correlation is significantly alleviated by incorporating the $A_{LU}^{\sin\phi}$ asymmetry. For the EIC, we assume 70% polarization of the electron beam [47]. Under this setup, single-operator constraints can reach the $\mathcal{O}(0.01) \sim \mathcal{O}(0.1)$ level. Importantly, while $A_{LU}^{\sin\phi}$ retains strong correlations between coefficients, the orientation of the corresponding blue band is different from that of $A_{UU}^{\sin\phi}$. Their combination thus greatly improves the parameter space resolution, confining the allowed region to a narrow area highlighted in red. Similar improvements are also observed in the constraints on C_{dW} - C_{dB} and $c_{q\gamma}$ - c_{qZ} (see Supplemental Material [51]). The constraints on the imaginary parts can be obtained analogously from the $\cos\phi$ -asymmetry, yielding identical sensitivities. These results underscore the strong capability of the proposed asymmetries to unveil light-quark dipole interactions at the EIC.

Besides the future EIC, the absence of a polarized nucleon beam requirement for these asymmetries also opens up opportunities to use available data from HERA. In Fig. 3, we compare the projected sensitivity from the combined-asymmetry analysis among the EIC, HERA [53], and the LHeC [54]. Although HERA benefits from higher- Q^2 coverage, its lower luminosity results in slightly weaker sensitivity compared to the EIC. However, it provides better discrimination between operators. With even higher energy and better luminosity, the LHeC could outperform both HERA and EIC by an order of magnitude.

Conclusion and discussion In summary, we have shown that nucleon energy correlators (NECs) provide a powerful framework to probe EW light-quark dipole operators

in inclusive DIS with an unpolarized nucleon. By exploiting azimuthal correlations of the energy flux in the TFR, we introduce a chiral-odd NEC sensitive to the transverse spin of quarks, even within an unpolarized target. Coupling to the interference between the dipole and SM amplitudes, the transversity NEC produces characteristic $\sin\phi$ and $\cos\phi$ asymmetries in the energy pattern, providing clean access to the dipole couplings. Our combined analysis with both unpolarized and longitudinally polarized electron beams demonstrates that these observables can deliver precise and complementary constraints at the EIC.

This work initiates an exploration of energy-correlator observables in the search for new physics (for an effort in other directions, see [55]). Compared with proposals based on transversity PDFs or dihadron production [16, 18], our NEC-based approach eliminates the need for nucleon polarization and relies entirely on inclusive calorimetric measurements, without particle identification or hadron reconstruction. These features simplify experimental implementation and reduce statistical uncertainties. They also enable the full utilization of high luminosity from the future EIC and LHeC as well as the use of existing HERA data. Furthermore, the resulting constraints might benefit from extensions to heavy-ion beams.

While the present study employs inclusive NECs, improved angular resolution could be achieved through track-based measurements of charged-hadron energy flux [56–59], which would be valuable for precision studies on the dipole couplings. Furthermore, the chiral-odd NEC framework can be extended to polarized nucleons, with all such NECs sharing identical hard-scattering kernels, thus offering robust and complementary constraints. Beyond DIS, NECs could also be applied to processes such as Drell–Yan production at the LHC. Detailed investigations along these lines are left for future work.

Acknowledgments We thank Yu Jia, Yi Liao, Xiaohui Liu, Jianping Ma, Hongxi Xing for helpful discussions and comments. X.B. Tong is supported by the Research Council of Finland, the Centre of Excellence in Quark Matter and projects 338263 and 359902, and by the European Research Council (ERC, grant agreements No. ERC-2023-101123801 GlueSatLight and No. ERC-2018-ADG-835105 YoctoLHC). H. L. Wang is supported by the Grants No. NSFC-12247151. The content of this article does not reflect the official opinion of the European Union and responsibility for the information and views expressed therein lies entirely with the authors.

* yingsheng.huang@outlook.com

† xuan.bo.tong@jyu.fi

‡ whaolin@m.scnu.edu.cn

- [1] W. Buchmuller and D. Wyler, *Effective Lagrangian Analysis of New Interactions and Flavor Conservation*, *Nucl. Phys. B* **268** (1986) 621.
- [2] C. Arzt, M.B. Einhorn and J. Wudka, *Patterns of deviation from the standard model*, *Nucl. Phys. B* **433** (1995) 41 [[hep-ph/9405214](#)].
- [3] B. Grzadkowski, M. Iskrzynski, M. Misiak and J. Rosiek, *Dimension-Six Terms in the Standard Model Lagrangian*, *JHEP* **10** (2010) 085 [[1008.4884](#)].
- [4] R. Alonso, E.E. Jenkins, A.V. Manohar and M. Trott, *Renormalization group evolution of the standard model dimension six operators iii: Gauge coupling dependence and phenomenology*, *JHEP* **04** (2014) 159 [[1312.2014](#)].
- [5] J. Kley, T. Theil, E. Venturini and A. Weiler, *Electric dipole moments at one-loop in the dimension-6 smeft*, *Eur. Phys. J. C* **82** (2022) 926 [[2109.15085](#)].
- [6] J. Aebischer, W. Dekens, E.E. Jenkins, A.V. Manohar, D. Sengupta and P. Stoffer, *Effective field theory interpretation of lepton magnetic and electric dipole moments*, *JHEP* **07** (2021) 107 [[2102.08954](#)].
- [7] M. Ardu and N. Valori, *The equivalent electric dipole moment in smeft*, [2503.21920](#).
- [8] R. Boughezal, E. Mereghetti and F. Petriello, *Dilepton production in the SMEFT at $O(1/\Lambda^4)$* , *Phys. Rev. D* **104** (2021) 095022 [[2106.05337](#)].
- [9] L. Allwicher, D.A. Faroughy, F. Jaffredo, O. Sumensari and F. Wilsch, *Drell-Yan tails beyond the Standard Model*, *JHEP* **03** (2023) 064 [[2207.10714](#)].
- [10] E. da Silva Almeida, N. Rosa-Agostinho, O.J.P. Éboli and M.C. Gonzalez-Garcia, *Light-quark dipole operators at the LHC*, *Phys. Rev. D* **100** (2019) 013003 [[1905.05187](#)].
- [11] X. Li, B. Yan and C.P. Yuan, *Lam-tung relation breaking in z boson production as a probe of standard model effective field theory effects*, *Phys. Rev. D* **111** (2025) 073007 [[2405.04069](#)].
- [12] R. Gauld, U. Haisch and J. Weiss, *A tale of Z -jet: SMEFT effects and the Lam-Tung relation*, *SciPost Phys.* **18** (2025) 148 [[2412.13014](#)].
- [13] G. Li, X. Li and B. Yan, *Lam-tung relation breaking effects and weak dipole moments at lepton colliders*, [2503.17663](#).
- [14] R. Escribano and E. Masso, *Constraints on fermion magnetic and electric moments from LEP-1*, *Nucl. Phys. B* **429** (1994) 19 [[hep-ph/9403304](#)].
- [15] G. Kopp, D. Schaile, M. Spira and P.M. Zerwas, *Bounds on radii and magnetic dipole moments of quarks and leptons from LEP, SLC and HERA*, *Z. Phys. C* **65** (1995) 545 [[hep-ph/9409457](#)].
- [16] R. Boughezal, D. de Florian, F. Petriello and W. Vogelsang, *Transverse spin asymmetries at the EIC as a probe of anomalous electric and magnetic dipole moments*, *Phys. Rev. D* **107** (2023) 075028 [[2301.02304](#)].
- [17] X.-K. Wen, B. Yan, Z. Yu and C.P. Yuan, *Single Transverse Spin Asymmetry as a New Probe of SMEFT Dipole Operators*, *Phys. Rev. Lett.* **131** (2023) 241801 [[2307.05236](#)].
- [18] X.-K. Wen, B. Yan, Z. Yu and C.P. Yuan, *Dihadron azimuthal asymmetry and light-quark dipole moments at the Electron-Ion Collider*, [2408.07255](#).
- [19] X.-K. Wen, B. Yan, Z. Yu and C.P. Yuan, *Transverse spin effects and light-quark dipole moments at lepton colliders*, [2411.13845](#).
- [20] M.B. Hecht, C.D. Roberts and S.M. Schmidt, *Neutron electric dipole moment: Constituent dressing and compositeness*, *Phys. Rev. C* **64** (2001) 025204 [[nucl-th/0101058](#)].
- [21] M. Pitschmann, C.-Y. Seng, C.D. Roberts and S.M. Schmidt, *Nucleon tensor charges and electric dipole moments*, *Phys. Rev. D* **91** (2015) 074004 [[1411.2052](#)].
- [22] T. Liu, Z. Zhao and H. Gao, *Experimental constraint on quark electric dipole moments*, *Phys. Rev. D* **97** (2018) 074018 [[1704.00113](#)].
- [23] T. Fukuyama, *Searching for new physics beyond the standard model in electric dipole moment*, *Int. J. Mod. Phys. A* **27** (2012) 1230015 [[1201.4252](#)].
- [24] T. Bhattacharya, V. Cirigliano and R. Gupta, *Neutron Electric Dipole Moment from Beyond the Standard Model*, *PoS LATTICE2012* (2012) 179 [[1212.4918](#)].
- [25] T. Chupp, P. Fierlinger, M. Ramsey-Musolf and J. Singh, *Electric dipole moments of atoms, molecules, nuclei, and particles*, *Rev. Mod. Phys.* **91** (2019) 015001 [[1710.02504](#)].
- [26] R. Alarcon et al., *Electric dipole moments and the search for new physics*, in *Snowmass 2021*, 3, 2022 [[2203.08103](#)].
- [27] A. Keshavarzi, K.S. Khaw and T. Yoshioka, *Muon $g - 2$: A review*, *Nucl. Phys. B* **975** (2022) 115675 [[2106.06723](#)].
- [28] G.A. González-Sprinberg, *Electric and magnetic tau dipole moments revisited*, in *17th International Workshop on Tau Lepton Physics*, 6, 2024, DOI [[2406.15286](#)].
- [29] B. Abi, T. Albahri, S. Al-Kilani, D. Allspach, L. Alonzi, A. Anastasi et al., *Measurement of the positive muon anomalous magnetic moment to 0.46 ppm*, *Physical Review Letters* **126** (2021) 141801 [[2104.03281](#)].
- [30] MUON G-2 collaboration, *Measurement of the Positive Muon Anomalous Magnetic Moment to 127 ppb*, [2506.03069](#).
- [31] R. Aliberti et al., *The anomalous magnetic moment of the muon in the Standard Model: an update*, [2505.21476](#).
- [32] BESIII collaboration, *Precise Measurement of the Λ Electric Dipole Moment through the Entangled Strange Baryon-Antibaryon System*, [2506.19180](#).
- [33] ACME collaboration, *Improved limit on the electric dipole moment of the electron*, *Nature* **562** (2018) 355.
- [34] X. Fan, T.G. Myers, B.A.D. Sukra and G. Gabrielse, *Measurement of the electron magnetic moment*, *Phys. Rev. Lett.* **130** (2023) 071801 [[2209.13084](#)].
- [35] C. Abel et al., *Measurement of the permanent electric dipole moment of the neutron*, *Phys. Rev. Lett.* **124** (2020) 081803 [[2001.11966](#)].
- [36] H.-L. Wang, X.-K. Wen, H. Xing and B. Yan, *Probing the four-fermion operators via the transverse double spin asymmetry at the Electron-Ion Collider*, *Phys. Rev. D* **109** (2024) 095025 [[2401.08419](#)].
- [37] X. Liu and H.X. Zhu, *Nucleon Energy Correlators*, *Phys. Rev. Lett.* **130** (2023) 091901 [[2209.02080](#)].
- [38] H. Cao, X. Liu and H.X. Zhu, *Toward precision measurements of nucleon energy correlators in lepton-nucleon collisions*, *Phys. Rev. D* **107** (2023) 114008 [[2303.01530](#)].
- [39] H. Cao, H.T. Li and Z. Mi, *Bjorken x weighted*

- energy-energy correlators from the target fragmentation region to the current fragmentation region, *Phys. Rev. D* **109** (2024) 096004 [2312.07655].
- [40] H.-Y. Liu, X. Liu, J.-C. Pan, F. Yuan and H.X. Zhu, Nucleon Energy Correlators for the Color Glass Condensate, *Phys. Rev. Lett.* **130** (2023) 181901 [2301.01788].
- [41] X. Liu and H.X. Zhu, TMDs from Semi-inclusive Energy Correlators, **2403.08874**.
- [42] K.-B. Chen, J.-P. Ma and X.-B. Tong, The connection between nucleon energy correlators and fracture functions, *JHEP* **08** (2024) 227 [2406.08559].
- [43] H. Mäntysaari, Y. Tawabutr and X.-B. Tong, Nucleon Energy Correlators for the Odderon, **2503.20157**.
- [44] X.L. Li, X. Liu, F. Yuan and H.X. Zhu, Illuminating nucleon-gluon interference via calorimetric asymmetry, *Phys. Rev. D* **108** (2023) L091502 [2308.10942].
- [45] Y. Guo, X. Liu, F. Yuan and H.X. Zhu, Long-Range Azimuthal Correlation, Entanglement, and Bell Inequality Violation by Spinning Gluons at the Large Hadron Collider, *Research* **2025** (2025) 0552 [2406.05880].
- [46] Y. Guo, X. Liu and F. Yuan, Long Range Energy-energy Correlator at the LHC, **2408.14693**.
- [47] R. Abdul Khalek et al., Science Requirements and Detector Concepts for the Electron-Ion Collider: EIC Yellow Report, *Nucl. Phys. A* **1026** (2022) 122447 [2103.05419].
- [48] N.A. Sveshnikov and F.V. Tkachov, Jets and quantum field theory, *Phys. Lett. B* **382** (1996) 403 [hep-ph/9512370].
- [49] C.W. Bauer, S.P. Fleming, C. Lee and G.F. Sterman, Factorization of e^+e^- Event Shape Distributions with Hadronic Final States in Soft Collinear Effective Theory, *Phys. Rev. D* **78** (2008) 034027 [0801.4569].
- [50] R.L. Jaffe and X.-D. Ji, Chiral odd parton distributions and Drell-Yan processes, *Nucl. Phys. B* **375** (1992) 527.
- [51] Y. Huang, X.-B. Tong and H.-L. Wang, Supplemental material, .
- [52] V. Barone, S. Melis and A. Prokudin, The Boer-Mulders effect in unpolarized SIDIS: An Analysis of the COMPASS and HERMES data on the $\cos 2\phi$ asymmetry, *Phys. Rev. D* **81** (2010) 114026 [0912.5194].
- [53] M. Klein and R. Yoshida, Collider physics at hermes, *Prog. Part. Nucl. Phys.* **61** (2008) 343 [0805.3334].
- [54] LHeC, FCC-HE STUDY GROUP collaboration, The Large Hadron-Electron Collider at the HL-LHC, *J. Phys. G* **48** (2021) 110501 [2007.14491].
- [55] L. Ricci and M. Riembau, Energy correlators of hadronically decaying electroweak bosons, *Phys. Rev. D* **106** (2022) 114010 [2207.03511].
- [56] H. Chen, I. Moult, X. Zhang and H.X. Zhu, Rethinking jets with energy correlators: Tracks, resummation, and analytic continuation, *Phys. Rev. D* **102** (2020) 054012 [2004.11381].
- [57] Y. Li, I. Moult, S.S. van Velzen, W.J. Waalewijn and H.X. Zhu, Extending Precision Perturbative QCD with Track Functions, *Phys. Rev. Lett.* **128** (2022) 182001 [2108.01674].
- [58] M. Jaarsma, Y. Li, I. Moult, W.J. Waalewijn and H.X. Zhu, Energy correlators on tracks: resummation and non-perturbative effects, *JHEP* **12** (2023) 087 [2307.15739].
- [59] K. Lee and I. Moult, Energy Correlators Taking Charge, **2308.00746**.
- [60] Z. Lu and I. Schmidt, Updating Boer-Mulders functions from unpolarized pd and pp Drell-Yan data, *Phys. Rev. D* **81** (2010) 034023 [0912.2031].
- [61] H1, ZEUS collaboration, Combination of measurements of inclusive deep inelastic $e^\pm p$ scattering cross sections and QCD analysis of HERA data, *Eur. Phys. J. C* **75** (2015) 580 [1506.06042].
- [62] C. Diaconu, T. Haas, M. Medinnis, K. Rith and A. Wagner, Physics accomplishments of hermes, *Ann. Rev. Nucl. Part. Sci.* **60** (2010) 101.

Supplemental material for “Nucleon energy correlators as a probe of light-quark dipole operators at the EIC”

Yingsheng Huang,^{*} Xuan-Bo Tong,[†] and Hao-Lin Wang[‡]

Appendix A: The complete results for energy-pattern cross section in the SM and SMEFT

Here we summarize the complete results for the energy-pattern cross section in the SM and SMEFT. In this work, we consider the case, where the target nucleon is unpolarized and the electron beam is unpolarized or longitudinally polarized. We are interested in the following components:

$$\Sigma(\theta, \phi) = \Sigma_{UU}(\theta) + \Sigma_{UU}^{\sin \phi}(\theta) \sin \phi + \Sigma_{UU}^{\cos \phi}(\theta) \cos \phi + \lambda_e [\Sigma_{LU}^{\sin \phi}(\theta) \sin \phi + \Sigma_{LU}^{\cos \phi}(\theta) \cos \phi],$$

where the first and second subscripts denote the polarizations of the electron beam and the nucleon target, respectively. λ_e denotes the helicity of the electron beam. In the TFR, these energy-pattern cross sections can be factorized in terms of the associated NECs. The following results are given in the leading order of α_s , and we have included all contributions from photon and Z boson exchanges.

In the SM, only azimuthal-symmetric cross section exists and is yielded by the unpolarized quark NEC $f_1^q(x_B, \theta^2)$:

$$\begin{aligned} \frac{d\Sigma_{UU}}{dx_B dQ^2} &= \frac{2\pi\alpha_{\text{em}}^2}{Q^4} \sum_q f_1^q(x_B, \theta^2) \left\{ Q_q^2(y^2 - 2y + 2) + \frac{2Q^2}{Q^2 + m_Z^2} \frac{Q_q}{(c_W s_W)^2} [g_A^e g_A^q(y - 2)y - g_V^e g_V^q(y^2 - 2y + 2)] \right. \\ &\quad \left. + \frac{1}{(c_W s_W)^4} \left(\frac{Q^2}{Q^2 + m_Z^2} \right)^2 [(y^2 - 2y + 2)[(g_A^e)^2 + (g_V^e)^2][(g_A^q)^2 + (g_V^q)^2] - 4y(y - 2)g_A^e g_A^q g_V^e g_V^q] \right\}. \quad (\text{A1}) \end{aligned}$$

In the SMEFT, the ϕ -dependent cross sections with unpolarized and longitudinally polarized electrons are given by the dipole couplings and the quark transversity NEC $h_1^{t,q}(x_B, \theta^2)$. For convenience, we present the results in mass basis:

$$\mathcal{L} = c_{q\gamma} (\bar{q}_L \sigma_{\mu\nu} q_R) F^{\mu\nu} + c_{qZ} (\bar{q}_L \sigma_{\mu\nu} q_R) Z^{\mu\nu} + \text{h.c.}, \quad (\text{A2})$$

where $q = u, d$ denote the up and down quarks. The dipole couplings c_i are related to the dimensionless Wilson coefficients C_i by

$$\begin{aligned} c_{q\gamma} &= (v/\sqrt{2}\Lambda^2) (c_W C_{qB} \pm s_W C_{qW}), \\ c_{qZ} &= (v/\sqrt{2}\Lambda^2) (-s_W C_{qB} \pm c_W C_{qW}), \end{aligned} \quad (\text{A3})$$

where the plus (minus) sign is for the up (down) quark, and v is the Higgs vacuum expectation value. The results are summarized as follows:

$$\begin{aligned} \frac{d\Sigma_{UU}^{\sin \phi}}{dx_B dQ^2} &= \frac{4\pi\alpha_{\text{em}}^2}{ec_W s_W} \frac{y\sqrt{1-y}}{Q(Q^2 + m_Z^2)} \sum_q h_1^{t,q}(x_B, \theta^2) \left\{ \left[\frac{2-y}{y} g_A^q g_V^e + g_V^q g_A^e \right] \frac{\text{Re}[c_{q\gamma}]}{c_W s_W} - Q_q g_A^e \text{Re}[c_{qZ}] \right. \\ &\quad \left. + \frac{1}{(c_W s_W)^2} \frac{Q^2}{Q^2 + m_Z^2} \left[\frac{2-y}{y} [(g_A^e)^2 + (g_V^e)^2] g_A^q + 2g_A^e g_V^e g_V^q \right] \text{Re}[c_{qZ}] \right\}, \quad (\text{A4}) \end{aligned}$$

$$\begin{aligned} \frac{d\Sigma_{LU}^{\sin \phi}}{dx_B dQ^2} &= \frac{4\pi\alpha_{\text{em}}^2}{Q^3} \frac{y\sqrt{1-y}}{e} \sum_q h_1^{t,q}(x_B, \theta) \\ &\quad \times \left\{ Q_q \text{Re}[c_{q\gamma}] - \frac{Q^2}{Q^2 + m_Z^2} \frac{1}{c_W s_W} \left[\left[\frac{2-y}{y} g_A^q g_A^e + g_V^q g_V^e \right] \frac{\text{Re}[c_{q\gamma}]}{c_W s_W} - Q_q g_V^e \text{Re}[c_{qZ}] \right] \right. \\ &\quad \left. - \frac{1}{(c_W s_W)^3} \left(\frac{Q^2}{Q^2 + m_Z^2} \right)^2 [(g_A^e)^2 + (g_V^e)^2] g_V^q + \frac{2(2-y)}{y} g_A^e g_A^q g_V^e \right] \text{Re}[c_{qZ}] \right\}, \quad (\text{A5}) \end{aligned}$$

$$\frac{d\Sigma_{UU}^{\cos\phi}}{dx_B dQ^2} = -\frac{4\pi\alpha_{\text{em}}^2}{ec_W s_W} \frac{y\sqrt{1-y}}{Q(Q^2+m_Z^2)} \sum_q h_1^{t,q}(x_B, \theta^2) \left\{ \left[\frac{2-y}{y} g_A^q g_V^e + g_V^q g_A^e \right] \frac{\text{Im}[c_{q\gamma}]}{c_W s_W} - Q_q g_A^e \text{Im}[c_{qZ}] \right. \\ \left. + \frac{1}{(c_W s_W)^2} \frac{Q^2}{Q^2+m_Z^2} \left[\frac{2-y}{y} [(g_A^e)^2 + (g_V^e)^2] g_A^q + 2g_A^e g_V^e g_V^q \right] \text{Im}[c_{qZ}] \right\}, \quad (\text{A6})$$

$$\frac{d\Sigma_{LU}^{\cos\phi}}{dx_B dQ^2} = -\frac{4\pi\alpha_{\text{em}}^2}{Q^3} \frac{y\sqrt{1-y}}{e} \sum_q h_1^{t,q}(x_B, \theta) \\ \times \left\{ Q_q \text{Im}[c_{q\gamma}] - \frac{Q^2}{Q^2+m_Z^2} \frac{1}{c_W s_W} \left[\frac{2-y}{y} g_A^q g_V^e + g_V^q g_A^e \right] \frac{\text{Im}[c_{q\gamma}]}{c_W s_W} - Q_q g_V^e \text{Im}[c_{qZ}] \right] \\ - \frac{1}{(c_W s_W)^3} \left(\frac{Q^2}{Q^2+m_Z^2} \right)^2 \left[[(g_A^e)^2 + (g_V^e)^2] g_V^q + \frac{2(2-y)}{y} g_A^e g_A^q g_V^e \right] \text{Im}[c_{qZ}] \right\}. \quad (\text{A7})$$

Similar to the case of unpolarized electrons, we can introduce the azimuthal angle asymmetry for longitudinally polarized electrons by incorporating the spin asymmetry in the definition:

$$A_{LU}^{\sin\phi} = \frac{\pi}{2} \frac{\Sigma(\sin\phi > 0)|_{\lambda_e=+1} - \Sigma(\sin\phi < 0)|_{\lambda_e=+1} - (\Sigma(\sin\phi > 0)|_{\lambda_e=-1} - \Sigma(\sin\phi < 0)|_{\lambda_e=-1})}{\Sigma(\sin\phi > 0)|_{\lambda_e=+1} + \Sigma(\sin\phi < 0)|_{\lambda_e=+1} + (\Sigma(\sin\phi > 0)|_{\lambda_e=-1} + \Sigma(\sin\phi < 0)|_{\lambda_e=-1})}, \quad (\text{A8})$$

where $\Sigma(\sin\phi > 0)$ represents the θ -weighted energy pattern cross section integrated over the region with $\sin\phi > 0$,

$$\Sigma(\sin\phi > 0) \equiv \int_{\theta_{\min}^2}^{\theta_{\max}^2} d\theta^2 |\sin\theta| \int_0^{2\pi} d\phi \Sigma(\theta, \phi) \Theta(\sin\phi). \quad (\text{A9})$$

The $A_{LU}^{\cos\phi}$ asymmetry can be defined in a similar manner.

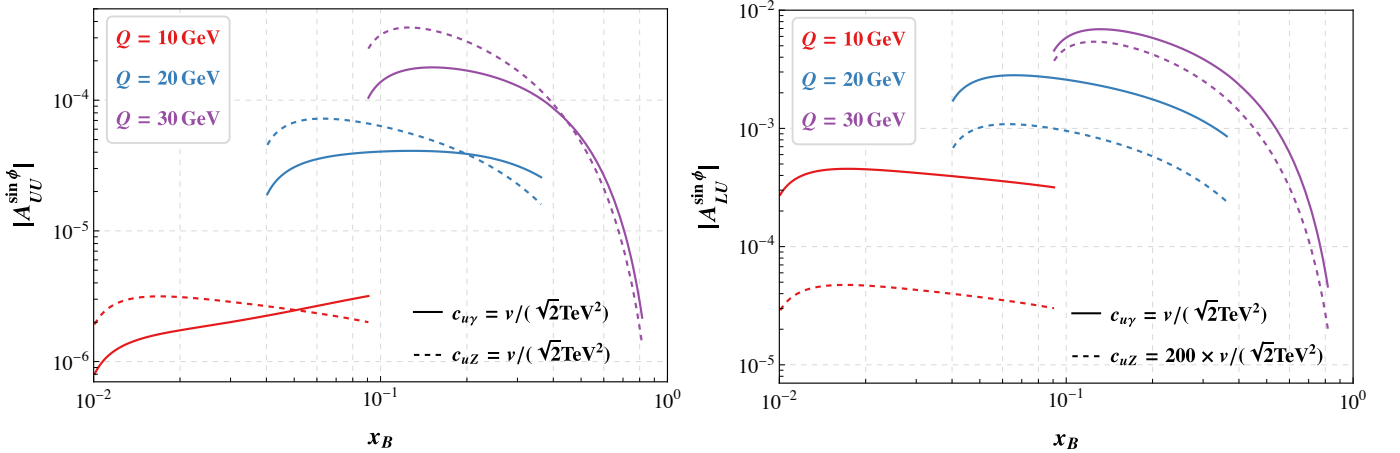


FIG. 4. $|A_{UU}^{\sin\phi}|$ (**Left**) and $|A_{LU}^{\sin\phi}|$ (**Right**) as a function of the Bjorken variable x_B for the up-quark dipole operators with different Q at the EIC. The solid (dashed) lines correspond to setting $c_{u\gamma}$ (c_{uZ}) = $v/(\sqrt{2} \text{ TeV}^2)$. The center-of-mass energy is set to be 105 GeV, and the inelasticity y is limited to $[0.1, 0.9]$.

For illustration, Fig. 4 shows the numerical results for $|A_{UU}^{\sin\phi}|$ and $|A_{LU}^{\sin\phi}|$ as a function of the Bjorken variable x_B for the up-quark dipole operators with different Q at the EIC kinematics. We take $\sqrt{s} = 105$ GeV to optimize luminosity and apply an inelasticity cut of $0.1 < y < 0.9$ [47]. The dimensionful dipole couplings are fixed to $c_{u\gamma} = v/(\sqrt{2} \text{ TeV}^2)$ for both asymmetries, with $c_{uZ} = v/(\sqrt{2} \text{ TeV}^2)$ for $|A_{UU}^{\sin\phi}|$ and $c_{uZ} = 200 v/(\sqrt{2} \text{ TeV}^2)$ for $|A_{LU}^{\sin\phi}|$ to enhance visibility. We find $A_{UU}^{\sin\phi} > 0$ for $c_{u\gamma}$ and $A_{UU}^{\sin\phi} < 0$ for c_{uZ} , while $A_{LU}^{\sin\phi} < 0$ for $c_{u\gamma}$ and $A_{LU}^{\sin\phi} > 0$ for c_{uZ} . The magnitude of both asymmetries grows with Q . In particular, $A_{LU}^{\sin\phi}$ from $c_{u\gamma}$ is free from the Q^2/m_Z^2 suppression, almost reaching $\mathcal{O}(10^{-2})$ at $Q = 30$ GeV. Results for d -quark operators follow a similar pattern, with slightly reduced magnitudes due to the smaller $h_1^{t,d}$. In our analysis, we use TMDs as the input for the NECs and apply the parameterization from [52]. The resulting asymmetries are consistent in magnitude with those obtained using the alternative fit in [60].

Appendix B: Additional constraints on the dipole operators at the EIC

In this section, we present the projected EIC sensitivities for d -quark dipole operators and for the dipole operators in the mass basis as given in Eq. (A2), providing complementary numerical results.

The constraints are derived from a χ^2 analysis, with χ^2 defined as

$$\chi^2 = \sum_i \left[\frac{A_{\text{th},i} - A_{\text{exp},i}}{\delta A_i} \right]^2, \quad (\text{B1})$$

where $A_{\text{th},i}$, $A_{\text{exp},i}$, and δA_i denote the theoretical prediction, experimental measurement, and statistical uncertainty of the asymmetry in the i -th bin, respectively. For the EIC, with the cuts: $0.1 \leq y \leq 0.9$ and $0.01 \leq x \leq 0.5$, we adopt different Q -binning schemes for A_{UU} and A_{LU} to account for their differing magnitudes. For A_{UU} , a fixed bin width of 10 GeV is used over the range $Q \in [10, 60]$ GeV. In contrast, the A_{LU} distribution is divided into 5 GeV bins across $Q \in [10, 50]$ GeV, with an additional bin spanning $Q \in [50, 60]$ GeV.

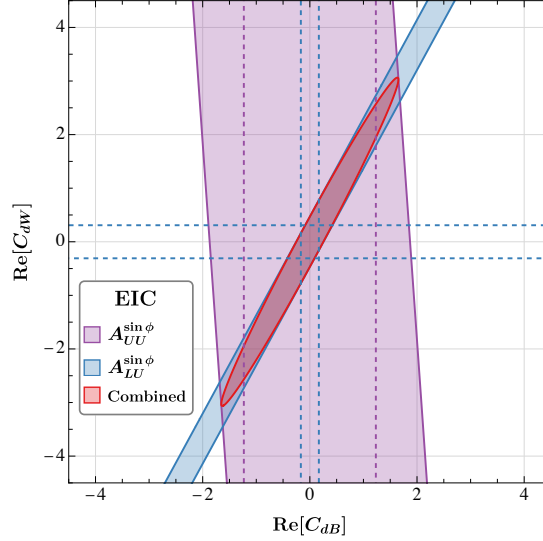


FIG. 5. Projected 68 % C.L. constraints at the EIC on the two Wilson coefficients $\text{Re}[C_{dB}]$ and $\text{Re}[C_{dW}]$, assuming $\Lambda = 1$ TeV. The limits are derived from the azimuthal asymmetries $A_{UU}^{\sin\phi}$ (purple), $A_{LU}^{\sin\phi}$ (blue), and their combination (red). The shaded regions represent the simultaneous two-coefficient constraints, while dashed lines show the limits for a single coefficient.

The projected constraints on $(\text{Re}[C_{dB}], \text{Re}[C_{dW}])$ are presented in Fig. 5, and those on $(\text{Re}[C_{qZ}], \text{Re}[C_{q\gamma}])$ with $q = u, d$ are shown in Fig. 6. The latter couplings have been rescaled to dimensionless form via $C_{q\gamma(Z)} \equiv c_{q\gamma(Z)}/(v/\sqrt{2}\text{TeV}^2)$. The most stringent constraints from combining $A_{UU}^{\sin\phi}$ and $A_{LU}^{\sin\phi}$ are highlighted in red, reaching values in the range $\mathcal{O}(0.01) \sim \mathcal{O}(0.1)$ for $C_{q\gamma}$. Individual limits from single-operator (double-operator) analyzes using $A_{UU}^{\sin\phi}$ and $A_{LU}^{\sin\phi}$ are indicated by purple and blue dashed lines (shaded regions), respectively. In some cases, the single-operator sensitivity from either $A_{UU}^{\sin\phi}$ or $A_{LU}^{\sin\phi}$ is too weak to be displayed; for instance, no limit is shown for $\text{Re}[C_{dW}]$ from $A_{UU}^{\sin\phi}$. The similarity between the $(\text{Re}[C_{dZ}], \text{Re}[C_{d\gamma}])$ and $(\text{Re}[C_{uZ}], \text{Re}[C_{u\gamma}])$ constraints arises from their identical analytic dependence on the asymmetry expressions, as shown in Sec. A. Due to the relatively smaller transversity NEC for d -quark, the combined constraints on operators involving d -quark are approximately a factor of two weaker than those for u -quark operators.

Appendix C: Comparison of constraints among HERA, the EIC and the LHeC

In addition to the EIC, this study analyzes the sensitivity of two other electron-proton colliders: HERA [53, 62] and the Large Hadron-Electron Collider (LHeC) [54]. HERA is included since our setup does not require nucleon polarization, while the LHeC represents a future high-energy frontier with enhanced sensitivity to new physics. For our numerical analyzes, we specifically consider the Run 6 phase of the LHeC. The parameters for these colliders are summarized in Table I.

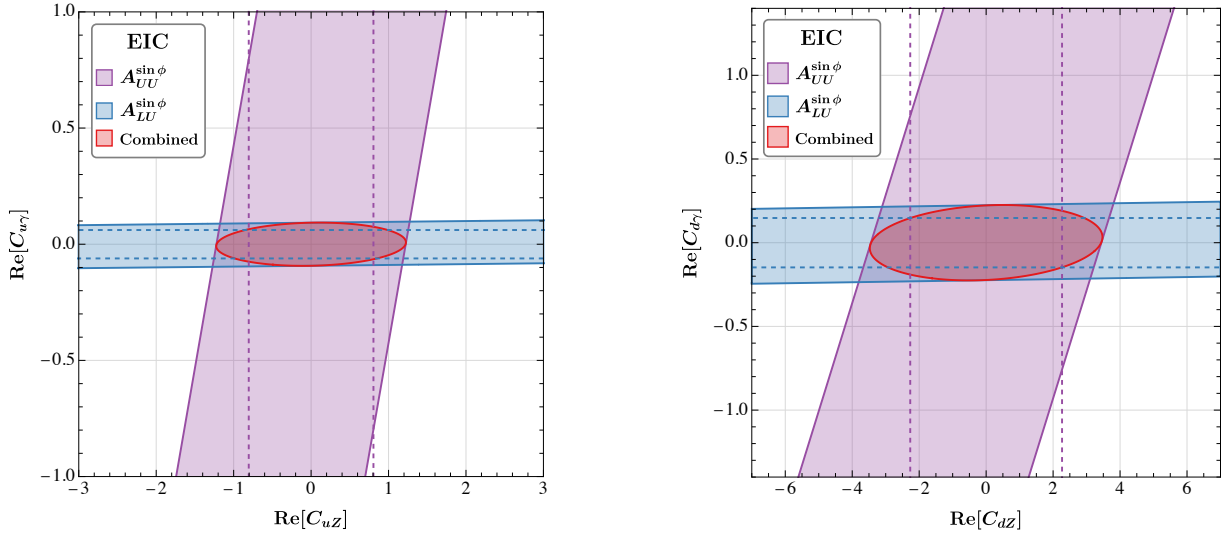


FIG. 6. Similar to Fig. 5, but for the dimensionless couplings $C_{q\gamma(Z)} \equiv c_{q\gamma(Z)}/(v/\sqrt{2}\text{TeV}^2)$.

Collider	\sqrt{s} [GeV]	\mathcal{L} [fb^{-1}]	P_e	Q [GeV]	y	x_B
EIC [47]	105	100	70%	[10, 60]	[0.1, 0.9]	[0.01, 0.5]
HERA [53, 61]	318	0.4	40%	[30, 150]	[0.1, 0.9]	[0.01, 0.5]
LHeC [54]	1300	50	80%	[100, 1000]	[0.1, 0.9]	[0.005, 0.9]

TABLE I. A summary of the experimental parameters and kinematic cuts for the three colliders considered in this analysis. The parameters shown are the center-of-mass energy (\sqrt{s}), the integrated luminosity (\mathcal{L}), and the degree of electron beam polarization (P_e). The ranges for the photon virtuality (Q), inelasticity (y), and Bjorken variable (x_B) are also specified.

We now present the numerical results for HERA and the LHeC. Following the procedure used for the EIC, we derive constraints on the real parts of the relevant dimension-6 Wilson coefficients from a χ^2 fit for the azimuthal asymmetries $A_{UU}^{\sin\phi}$ and $A_{LU}^{\sin\phi}$. This analysis is performed in Q bins. For the LHeC, we use intervals of 100 GeV over the range $100 < Q < 1000$ GeV, while for HERA, intervals of 10 GeV are used over the range $30 < Q < 150$ GeV. The kinematic cuts applied in our analysis are also detailed in Table I. The resulting projected constraints for HERA and the LHeC are presented in Fig. 7 and Fig. 8, respectively. These figures detail one-dimensional limits on individual operators and two-dimensional constraints on operator pairs involving both up and down quarks. These sensitivities are derived from fits using the $A_{UU}^{\sin\phi}$ and $A_{LU}^{\sin\phi}$ asymmetries individually, as well as from a combined fit. All constraints are presented in both the electroweak basis (e.g., C_{uB}, C_{uW}) and the mass basis (e.g., $C_{u\gamma}, C_{uZ}$).

Fig. 9 presents the final two-operator constraints from the EIC (red), HERA (green), and LHeC (blue) for a direct comparison. For visualization purposes, the LHeC ellipses are scaled by a factor of 10. The figure clearly illustrates the superior reach of the LHeC, a consequence of both its high center-of-mass energy and its large integrated luminosity. In contrast, HERA's potential is limited by its much smaller luminosity, though it still achieves a constraining power slightly weaker than that of the EIC thanks to its own high center-of-mass energy. Ultimately, both LHeC and HERA benefit from their access to a higher Q^2 range, resulting in similarly shaped constraining ellipses, whereas the EIC's limited Q^2 range induces stronger correlations between the coefficients.

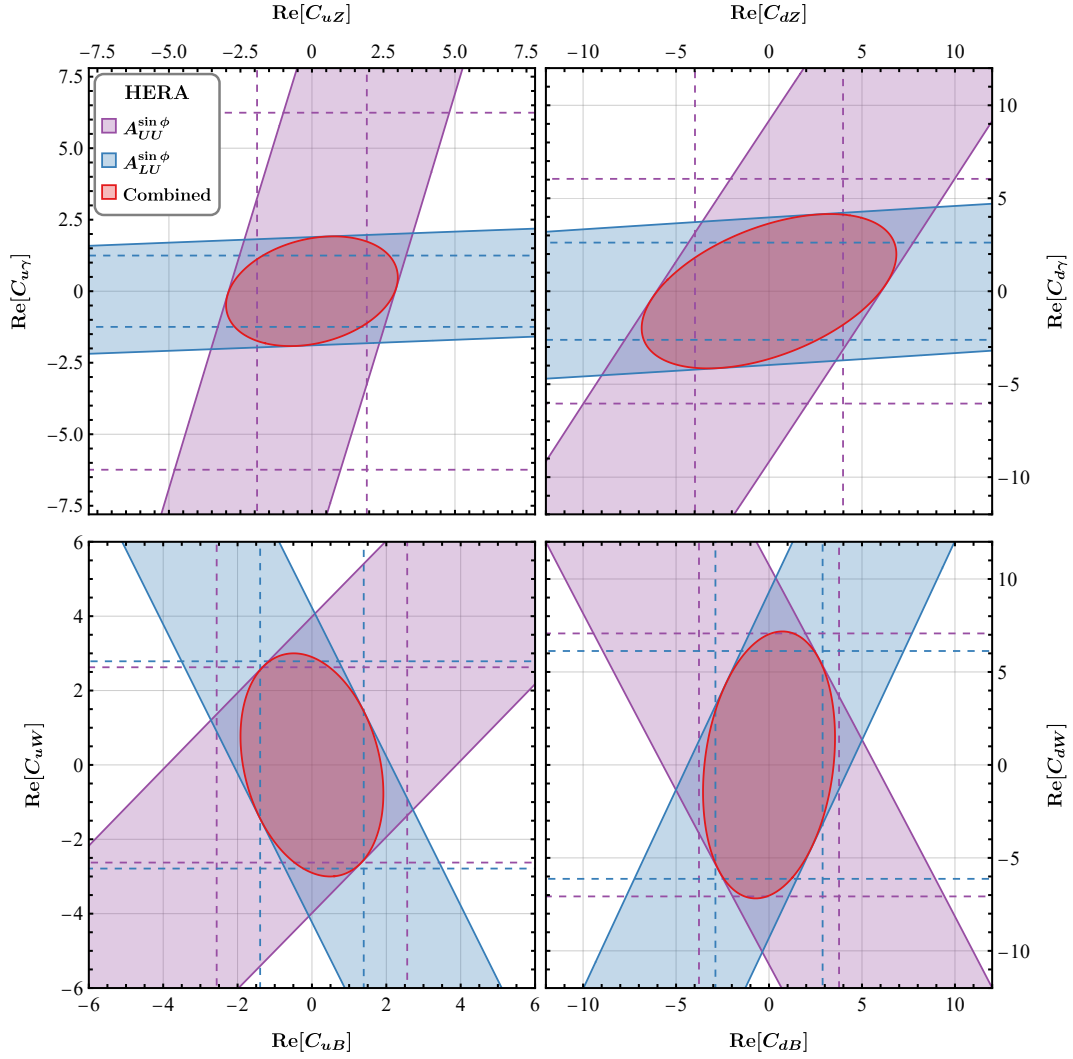


FIG. 7. The projected double-operator constraints at HERA with 68% C.L. on the real parts of the couplings, distinguishing between the up-channel (left column) and down-channel (right column). The top row shows constraints in the $\text{Re}[C_{q\gamma}]-\text{Re}[C_{qZ}]$ planes, while the bottom row shows the $\text{Re}[C_{qB}]-\text{Re}[C_{qW}]$ planes. All constraints are derived from the azimuthal asymmetries $A_{UU}^{\sin\phi}$ (purple) and $A_{LU}^{\sin\phi}$ (blue), assuming $\Lambda = 1$ TeV. The red ellipses represent constraints from combining $A_{UU}^{\sin\phi}$ and $A_{LU}^{\sin\phi}$. The dashed purple and blue lines correspond to the single-operator constraints from $A_{UU}^{\sin\phi}$ and $A_{LU}^{\sin\phi}$ respectively.

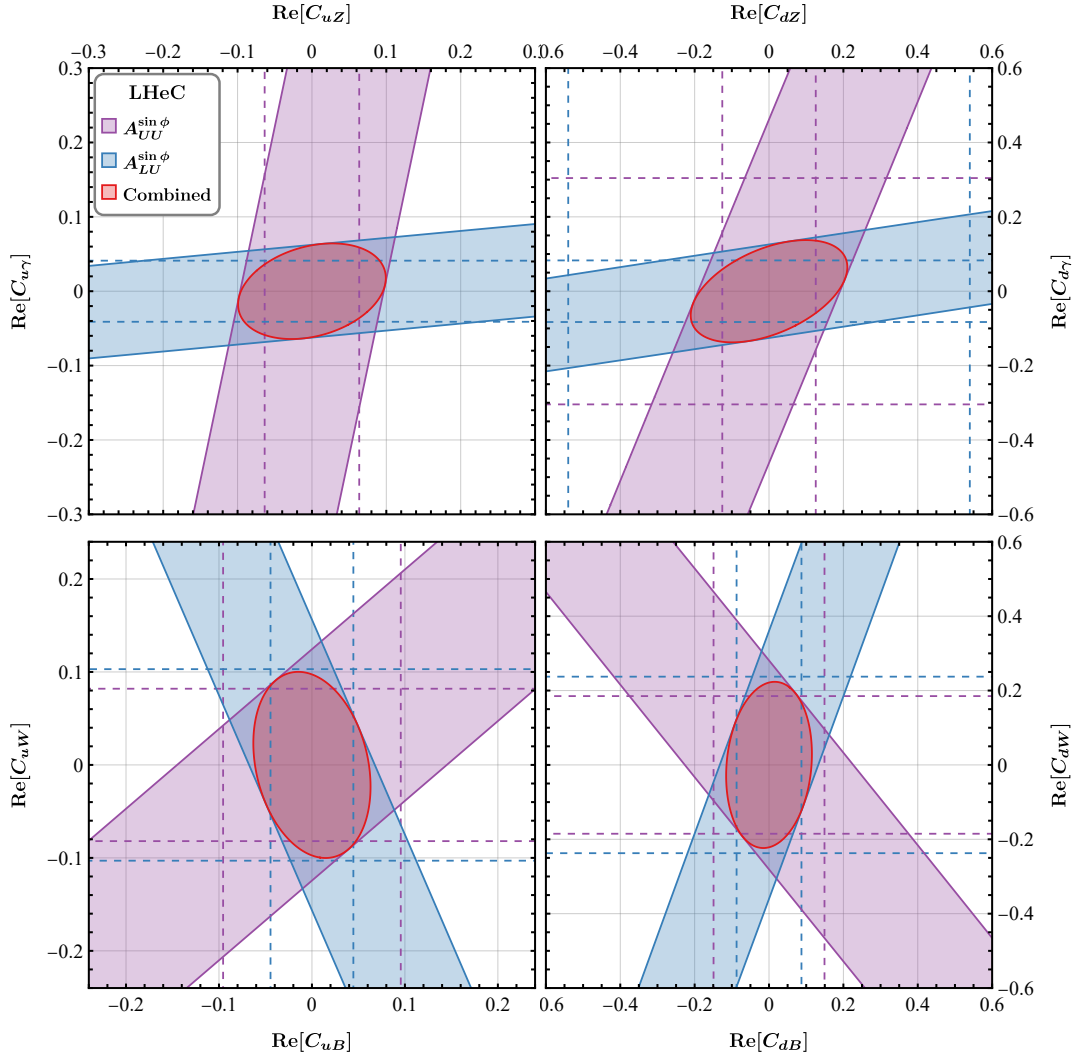


FIG. 8. The projected double-operator constraints at the LHeC with 68% C.L. on the real parts of the couplings, distinguishing between the up-channel (left column) and down-channel (right column). The top row shows constraints in the $\text{Re}[C_{q\gamma}]\text{-Re}[C_{qZ}]$ planes, while the bottom row shows the $\text{Re}[C_{qB}]\text{-Re}[C_{qW}]$ planes. All constraints are derived from the azimuthal asymmetries $A_{UU}^{\sin\phi}$ (purple) and $A_{LU}^{\sin\phi}$ (blue), assuming $\Lambda = 1$ TeV. The red ellipses represent constraints from combining $A_{UU}^{\sin\phi}$ and $A_{LU}^{\sin\phi}$. The dashed purple and blue lines correspond to the single-operator constraints from $A_{UU}^{\sin\phi}$ and $A_{LU}^{\sin\phi}$ respectively.

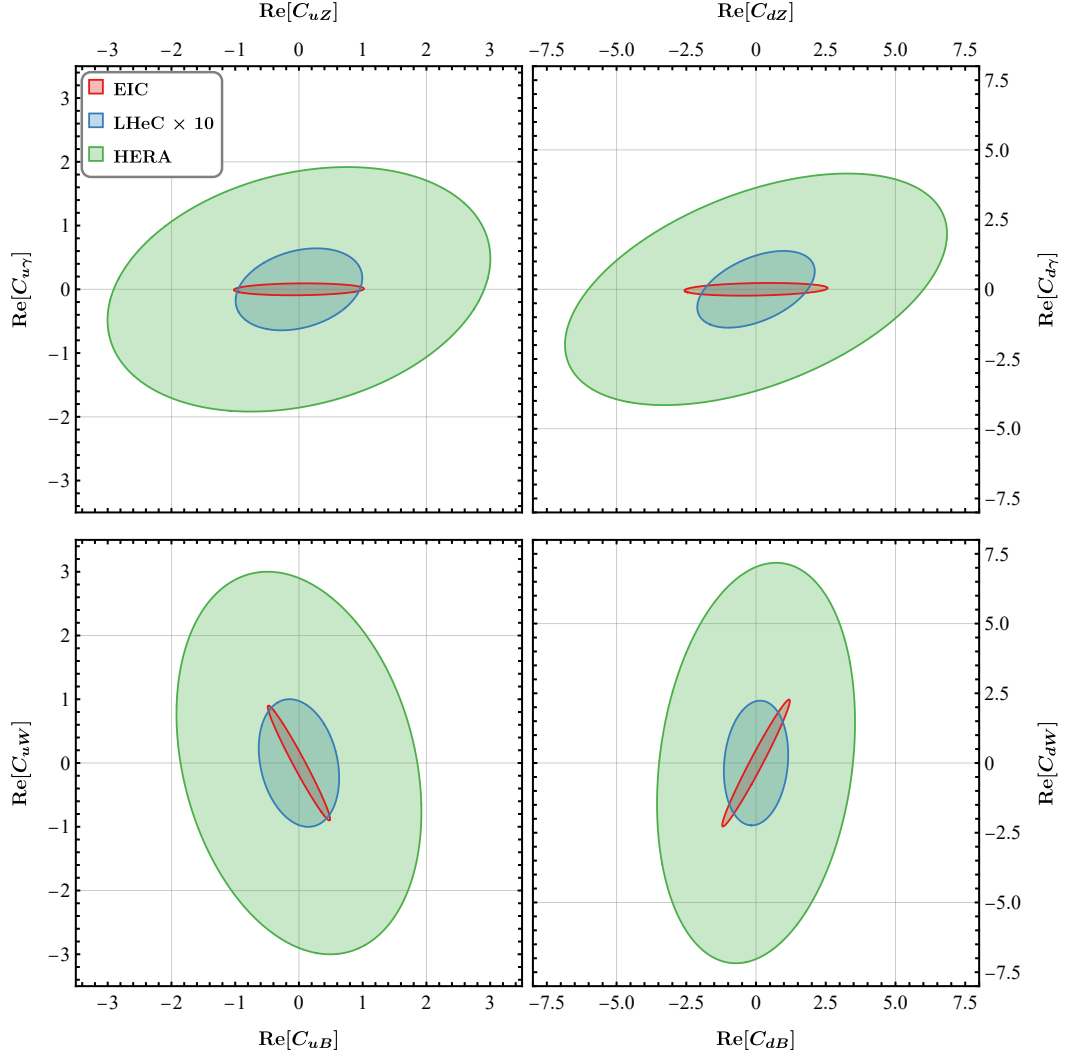


FIG. 9. Comparison of projected (EIC, LHeC) and existing (HERA) constraints at 68% C.L. on the real parts of the couplings, shown for the EIC (red), LHeC (blue, scaled by a factor of 10), and HERA (green). The layout distinguishes between the up-channel (left column) and down-channel (right column). The top row corresponds to the $\text{Re}[C_{q\gamma}]$ - $\text{Re}[C_{qZ}]$ planes and the bottom row corresponds to the $\text{Re}[C_{qB}]$ - $\text{Re}[C_{qW}]$ planes. Each contour represents a combined constraint derived from the azimuthal asymmetries $A_{UU}^{\sin\phi}$ and $A_{LU}^{\sin\phi}$, assuming $\Lambda = 1$ TeV.